PCCP

Fabrication, Thermal Analysis, and Heavy Ion Irradiation Resistance of Epoxy Matrix Nanocomposites Loaded with Silane-Functionalized Ceria Nanoparticles

SCHOLARONE™
Manuscripts

ARTICLE

Fabrication, Thermal Analysis, and Heavy Ion Irradiation Resistance of Epoxy Matrix Nanocomposites Loaded with Silane-Functionalized Ceria Nanoparticles

Clare Davis-Wheeler Chin,*[a] Marissa A. Ringgold,[a] Erica M. Redline,[b] Avi G. Bregman,[a] Khalid Hattar,[b] Amanda S. Peretti,[b] and LaRico J. Treadwell*[a]

This paper describes a detailed understanding of how nanofillers function as radiation barriers within the polymer matrix, and how their effectiveness is impacted by factors such as composition, size, loading, surface chemistry, and dispersion. We designed a comprehensive investigation of heavy ion irradiation resistance in epoxy matrix composites loaded with surface-modified ceria nanofillers, utilizing tandem computational and experimental methods to elucidate radiolytic damage processes and relate them to chemical and structural changes observed through thermal analysis, vibrational spectroscopy, and electron microscopy. A detailed mechanistic examination supported by FTIR spectroscopy data identified the bisphenol A moiety as a primary target for degradation reactions. Results of computational modeling by the Stopping Range of Ions in Matter (SRIM) Monte Carlo simulation were in good agreement with damage analysis from surface and cross-sectional SEM imaging. All metrics indicated that ceria nanofillers reduce the damage area in polymer nanocomposites, and that nanofiller loading and homogeneity of dispersion are key to effective damage prevention. The results of this study represent a significant pathway for engineered irradiation tolerance in a diverse array of polymer nanocomposite materials. Numerous areas of materials science can benefit from utilizing this facile and effective method to extend the reliability of polymer materials.

1. Introduction

Extending the reliability of polymer materials in extreme environments is crucial for ensuring the safe and consistent performance of components in nuclear reactors, spacecraft, and various protective coatings. Extreme environmental conditions such as temperature and ionizing radiation often lead to the irreversible degradation of essential material properties, creating a major barrier to materials selection for these applications.[1,2] Polymer materials are lightweight, have high mechanical stability, and enhance design flexibility for numerous applications in these fields.[3,4] However, their use has been limited by factors such as high susceptibility to irradiation damage and irreversible degradation of essential properties.

One promising strategy for overcoming these barriers involves engineering irradiation resistance through the addition of nanoscale filler materials. Polymer composites incorporating fillers such as nanoclays, carbon nanotubes, and block copolymers have attracted substantial interest across numerous scientific disciplines due to their enormous potential for performance enhancement and the introduction of novel, value-added thermal and mechanical properties.[5,6] Multiple studies have established that nanofillers provide a highly effective means to improve the mechanical strength, thermal stability, and durability of various polymers.[7,8] Their tunable motif, diverse composition, and versatile surface functionalization provide many opportunities to modify materials for case-specific applications.[9–12]

In particular, nanostructured epoxy matrix composites have emerged as key materials for achieving tailored responses to extreme environments due to their high irradiation tolerance.[13–15] Structural damage and property changes in nanofiller-loaded polymer matrix composites under various irradiation conditions have been well studied, especially for epoxy resins that are commonly used in nuclear energy applications.[16–18] However, the impacts of nanofillers on radiolytic damage processes within the polymer matrix are not well understood.[19–22] Building a detailed mechanistic understanding of heavy ion irradiation damage formation and recovery in nanostructured epoxy matrix composites is needed to guide the development of advanced materials solutions for applications in extreme environments.[4,18,23,24]

[a.] Advanced Materials Laboratory, Sandia National Laboratories, 1001 University Blvd. SE, Suite 100, Albuquerque, NM 87106, USA.
[b.] Sandia National Laboratories, P.O. Box 5800, Albuquerque, NM 87185, USA.
†Corresponding author: Dr. LaRico J. Treadwell. *Email:* ljtread@sandia.gov; *Tel.:* +1 (505) 389-3503; *Fax:* +1 (505) 284-3017.

1.1 Irradiation Damage in Polymer Materials

Polymer materials are highly susceptible to damage from heavy ion, gamma, and other ionizing irradiation that is often present in extreme environments. Ion beam irradiation studies of polymers and nanostructured composites can be used to elucidate damage mechanisms and drive the development of materials with enhanced irradiation resistance.[19–22] In particular, examining the effects of heavy ion irradiation is important for developing polymer materials to operate in space, where spacecraft and satellite components suffer severe damage accumulation from long-term exposure to solar and galactic cosmic rays containing energetic high-Z ions (HZE).[4] Large particle accelerators can generate HZE ion beams that selectively mimic real world irradiation conditions experienced during materials operation in various environments. HZE ions are also used to simulate neutron displacement damage in order to develop advanced materials for commercial nuclear energy applications.[4]

Computational modeling has recently emerged as a complementary method to HZE ion irradiation studies through prediction and validation of experimental data. Molecular dynamics (MD), density functional theory, and Monte Carlo simulations have been used to explore atomistic interactions between energetic ions, polymer matrix targets, and nanomaterial interfacial phenomena. These simulation techniques have been adopted for use with diverse materials and irradiation conditions to expand understanding of materials reliability in extreme environments and drive engineering of irradiation tolerant nanocomposites.

Rahmani et al. employed a reactive MD simulation to examine damage mitigation of nanoparticle-enhanced polymers under bombardment from atomic oxygen (AO), which poses significant hazards to spacecraft in low Earth and space missions.[25] Comparison of NP type and orientation revealed the most effective damage mitigation in composites with randomly oriented carbon nanotube and graphene NPs.

Ashraf et al. also used reactive MD simulations of AO bombardment to explore degradation resistance as a function of varying chemical composition in thermosetting epoxy polymers.[26] Their simulation results revealed that the curing agent with a stable aromatic ring significantly improved performance over composites with aliphatic and cycloaliphatic curing agents.

The cracking process of Bisphenol F epoxy resin under high energy particle impact was investigated by Xing et al., who used MD simulations to investigate cracking processes in Bisphenol F epoxy resins under the high energy particle impacts found in superconducting power equipment.[27] The simulations allowed elucidation of decomposition processes and mechanisms at the atomic scale.

1.1.1 HZE induced damage processes Energetic HZE undergo electrical interactions with target materials and can lose their kinetic energy through inelastic collisions with the electrons of target atoms.[23,28,29] Through electron-phonon coupling, the kinetic energy of ejected electrons is absorbed by the polymer backbone, generating heat and causing the ionization and excitation of target atoms along the path of the incident ion. Incident HZE can also interact via elastic collisions with the nuclei of target atoms, ejecting the target atom from its original position in the polymer and forming a displacement defect.[30] Both types of interactions are depth dependent, with kinetic energy dissipation into the target occurring close to the surface, while nuclear energy loss and displacement defects occur at greater depths.[30]

These interactions initiate a free radical mechanism that propagates damage via chain scission, crosslinking, and the emission of small molecules and fragments.[31] Active radicals can also be generated from the direct radiolytic cleavage of covalent bonds in the polymer matrix.[32] The damage induced by these processes can be observed as changes to the mechanical, electrical, and structural properties of irradiated polymers.[33]

1.1.2 Nanofiller effects When incorporated into a polymer matrix, nanofillers act as effective barriers against irradiation damage. This is often attributed to the nanofillers large surface volume fraction, which creates abundant areas of interfacial interaction with the polymer matrix.[31] These interfaces have been found to restrict the diffusion of activated atoms and radicals throughout the polymer matrix via trapping and scavenging processes.[29,34] The interfacial areas can promote covalent interactions between reactive amine and hydroxyl functions within the epoxy matrix and groups on the nanoparticle surface.

Previous studies have credited such interactions with a significant decrease in the yield of radiochemical degradation products.[35] Nanofiller interfaces can also absorb heat released by incident ions, diverting it away from the polymer backbone.[33,34,36–39] Visakh et al. observed that the addition of Al_2O_3 nanofillers decreased irradiation damage to epoxy matrices, which suffered depolymerization from thermal energy generated by radiolytic processes.[40]

Among the wide variety of nanofiller materials, ceria NPs have become known as uniquely suited to enhancing irradiation resistance of polymer materials.[41] The atomic structure of cerium facilitates an oxygen buffering process in which excess electrons left behind by radiolytically displaced oxygen atoms localize on the empty Ce $4f$ states, resulting in a valence change from Ce^{4+} to Ce^{3+}.[41] The reduction reaction generates oxygen vacancies within the ceria, creating an efficient and reversible pathway for scavenging of free oxygen radicals and slowing down radical-driven decomposition of polymer matrices under irradiation.[31,42–44]
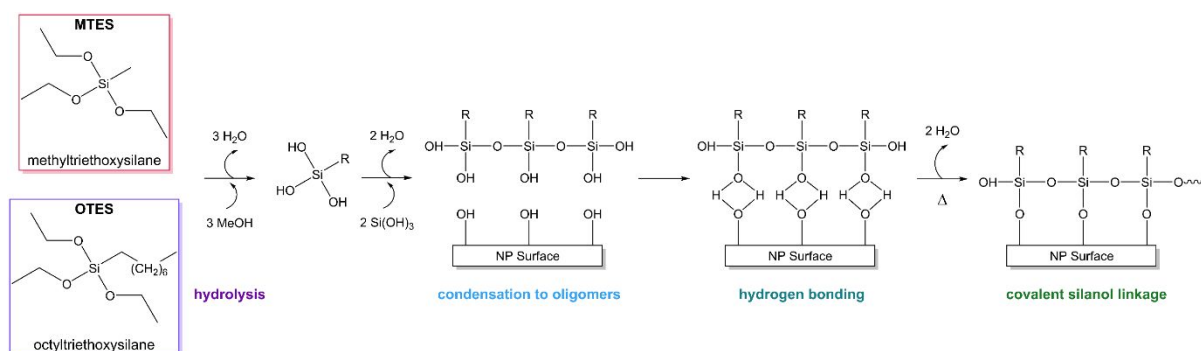
Scheme 1. Grafting of silane coupling agents to the surface of ceria nanoparticles.

1.2 Optimizing Polymer Nanocomposite Properties

The engineering of irradiation tolerance in nanocomposites must account for many factors that significantly affect material properties, such as the dispersion state,[37] geometric shape,[38] surface properties,[45] and particle average size and distribution of the nanofillers.[46] Nanocomposite properties can also be strongly affected by interactions between the nanoparticle (NP) fillers and the polymer, such as NP surface energy and chemistry, filler loading levels, and the characteristics of NP/polymer interfacial interactions. The large surface area of small nanoparticles significantly increases their interfacial interaction area within the polymer matrix.[47]

Achieving a tailored, whether homogeneous or graded, nanofiller dispersion is critical for optimizing these interactions.[48] Homogenous dispersion is often difficult to achieve and limited by the mismatch in hydrophobicity or polarity between the polymer and functional groups on the NP surface, as well as the tendency of nanoparticles to agglomerate. This can be resolved by using dually functional species like silane coupling agents (SCAs) to act as bridges spanning interphase regions that enable bonding between organic and inorganic substrates.[49]

SCAs have the general structure $(RO)_3–Si–R'–X$, where RO is an alkoxy or other hydrolysable group, R' is an alkyl linkage, and X is an organofunctional group that does not participate in coupling reactions.[49] Certain SCAs such as methyltriethoxysilane (MTES) and octyltriethoxysilane (OTES) (**Scheme 1**) are often grafted to nanofiller surfaces to facilitate their dispersion in epoxy and polyethylene matrices. Both feature three hydrolysable ethoxy groups for improved grafting ability to NPs, and are identical except for the OTES long alkyl chain.[50] The grafting reaction involves hydrolysis of the ethoxy groups to form reactive silanol species, which then react with NP surface hydroxyl groups to form a stable, covalent siloxane linkage.[51]

1.3 Fabrication and Heavy Ion Irradiation of Epoxy Resins Loaded with SCA–Ceria Nanofillers

In this work, we investigate the aging and degradation phenomena of epoxy nanocomposites exposed to high doses of HZE to support materials qualification, extend reliability,

and make technical contributions to production and development of HZE-protective materials. We present the fabrication, characterization, and heavy ion irradiation effects of epoxy nanocomposites with systematic variation of surface modification and loading level of ceria (CeO_2) nanofillers. Ceria nanofillers were chosen due to their established benefits to radiation attenuation, corrosion resistance, thermal stability, and mechanical properties in a wide variety of composite materials.[52,53] Two different SCAs were grafted to the surface of commercial CeO_2 NPs. The SCA-modified ceria nanofillers were used to fabricate amine crosslinked epoxy composites with nanofiller loading levels from 20–60 wt%. It was determined that SCA impacted particle dispersion and overall resistance to HZE.

Experimental and simulated damage conditions under heavy ion irradiation were used to investigate degradation pathways, determine dominant processes, and study the increase in reliability with respect to the inclusion of SCA-ceria nanofillers. Materials qualification as a function of nanofiller dispersion and loading was conducted by comparing the vibrational spectra and surface and cross-sectional electron micrographs for neat epoxy, low, and high nanofiller loading samples recorded before and after exposure to a heavy ion (20 MeV Au^{4+}) beam. Ion beam species, energy, and fluence were chosen to closely mimic real world extreme environmental conditions.

2. Experimental

2.1 Materials

Ethanol (EtOH) (200 proof, ACS Reagent, ≥99.5%), isopropyl alcohol (IPA) (ACS Reagent, ≥99.5%), methyltriethoxysilane (MTES) (99%), octyltriethoxysilane (OTES) (97%), and hydrochloric acid (37%, ACS Reagent) were purchased from Sigma Aldrich. Cerium(IV) oxide nanopowder (99.5%, 15 – 30 nm APS) and sodium hydroxide (25% solution) were purchased from Alfa Aesar. EPON™ liquid epoxy resin 828 was purchased from Hexion, Inc. Jeffamine® T403 (polyoxypropylenetriamine) was purchased from Huntsman Corp. All materials were used as received.

### 2.2 Grafting of silane coupling agents ceria NP surfaces

Silane surface functionalization of commercial ceria NPs was carried out according to the procedure by Palimi et al.[51,54] The mass of silane added (*M*) was calculated via **Equation 1**:

(2)
$$M = \frac{M_p \times S_s}{MSC}$$

Where M_p is the mass of nanoparticles (g), S_s is the nanoparticle surface area (m²/g), and *MSC* represents the constant for minimum surface coverage (436 m²/g).[51] A surface area value of 42 m²/g was used for the ceria NPs based on their average diameter of 20 nm. For 10 g ceria NPs, 0.96 g of silane would be required to achieve the minimum surface coverage. Previous studies have found that a fivefold increase over the minimum calculated silane mass gave optimal surface functionalization, and so 6.7 g of silane were used per 10 g ceria NPs in this study.[54]

Grafting of SCAs to hydroxylate groups on ceria NP surfaces was performed by combining 500 mL EtOH and 20 mL DI H_2O with 10 g of commercial ceria NPs in a 1000 mL three-neck flask. The mixture was adjusted to pH 2 by adding 37% HCl dropwise while stirring. 6.7 g of silane was then added to the mixture and magnetically stirred to disperse. The reaction mixture was heated to reflux at 80 °C and held for one hour to promote silane hydrolysis. After 1h, the pH was adjusted to 9 through dropwise addition of 6 M NaOH in order to promote condensation and attachment of the hydrolyzed silanes to the NPs surface. The reaction mixture was again heated to reflux at 80 °C and held for 2 hours, then cooled to room temperature. The product was separated via centrifugation and washed 6 times with IPA and DI H_2O, then dried in air overnight at 72 °C.

The formation of covalent linkages between SCAs and ceria NP surfaces is initiated by hydrolysis of the three labile alkoxy groups to form silanols, as seen for OTES in **Equation 2**:[49,55]

(3) $C_8H_{17}Si(OC_2H_5)_3 + 3H_2O \rightarrow C_8H_{17}Si(OH)_3 + 3C_2H_5OH$
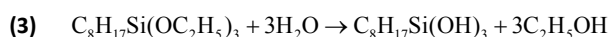
The silanols condense to form oligomers, which subsequently form hydrogen bonds with hydroxyl groups on the ceria NPs surface. **Equation 3** represents the formation of a covalent silanol linkage:

(4) $C_8H_{17}Si(OH)_3 + CeO_2-(OH) \rightarrow CeO_2-O-Si(OH)_2(C_8H_{17}) + H_2O$
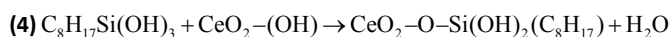
Scheme 1 summarizes this reaction sequence. The interface of the final product contains one covalent bond between the organosilane and the substrate, while the two remaining silanol groups can undergo condensation or remain free.[56]

2.3 Fabrication of SCA–NP/epoxy nanocomposites

SCA-capped ceria NPs (SCA–NPs) were added to pre-measured EPON-828 in 0.5 g increments and hand mixed. After each NP addition, the mixture was horn sonicated with a Branson horn sonicator at 50% amplitude at 5 second on, 5 second off intervals for a total of 10 minutes. The previous

two steps were repeated until the desired NP loading (20, 30, 40, 50, or 60 wt%) was reached and the NPs were fully incorporated. The curing agent, Jeffamine® T403, was then added to the mixture, which was then horn sonicated for 1 minute. Five drops of the degasser Shin-Etsu KF-105 were mixed in with a spatula. The mixture was then de-aired under dynamic vacuum at 60 °C for a maximum of 10 minutes. Finally, the mixture was poured or spread into silicone molds and cured at 80 °C for 10 hours. **Figure 1** shows the structures of the unmodified EPON-828 and Jeffamine® T-403 as well as that of the amine-crosslinked EPON-828 resin. Composite samples are referred to using "M" or "O" to denote MTES and OTES silane capping agents along with their weight percent loading (for example, M20 represents the MTES-capped NPs at a 20 wt% loading in the epoxy resin).
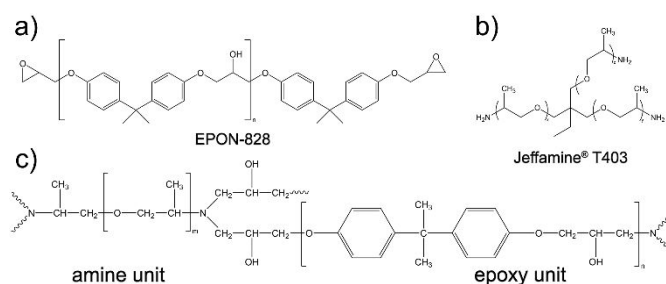

Figure 1. Structures of (a) EPON-828; (b) Jeffamine® T403; (c) amine-crosslinked epoxy network after curing.

2.4 Heavy ion irradiation

Ion irradiation was performed using 20 MeV Au^{4+} to a total dose of 10^{14} ion/cm² generated by the 6 MV HVEE Tandem Van de Graaff accelerator at Sandia National Laboratories. Samples were mounted on Si wafers with carbon tape and implanted at a base pressure 1×10^{-6} Torr or better vacuum. The ion beam was rastered to ensure spatially uniform irradiation damage and the ion flux was limited to minimize outgassing and significant temperature changes, which were monitored using an FLIR thermal imaging camera.

Computational modeling via the Stopping Range of Ions in Matter (SRIM 2013) Monte Carlo simulation was used to validate experimental observations of damage induced by heavy ion irradiation and gain insight into damage distribution.[57] The quick Kinchin-Pease calculation was used to simulate depth dependent damage accumulation and vacancy production for 50,000 incident 20 MeV Au ions at 0° angle of incidence to a 1-mm thick sample.[58] Threshold displacement energies (E_d) of 10, 28, 27, and 56 eV for H, C, O, and Ce (respectively) were adopted from molecular dynamics simulations.[59,60] Surface binding energies were taken from the SRIM database and lattice binding energies were set to zero.[61,62] SRIM simulations were run for the neat epoxy and nanocomposites with 20 and 60 wt% SCA–NP loadings based on stoichiometric atomic percentages of H, C, O, and Ce for each sample (Si was not included due to its very small value relative to the other elements). Damage estimation was reported as maximum and average ion

penetration depth and vacancy production per incident Au ion per Å.[58] A summary of SRIM input parameters is given in **Table S1**.

2.5 Characterization

For surface imaging via scanning electron microscopy (SEM), the samples were mounted with carbon tape on a Si wafer and characterized using a JEOL IT300HRLV SEM operated at 1 keV. Secondary electron images of uncoated samples were acquired in high vacuum mode to enhance image quality while minimizing charging effects from the electron beam. Cross-sectional scanning electron microscopy (XSEM) and EDS mapping (XEDS) were performed on an FEI Magellan 400 equipped with an Oxford ULTIM MAX EDS detector and Aztec 4.0 SP1 analysis software. Secondary electron images were collected at an operating voltage of 1 keV and a current of 13 pA, while XEDS mapping was performed at 5 keV and 3.2 pA. Samples were cryo-fractured and mounted vertically with the cracked side towards the camera on a 90° 25 mm aluminum stub. Experimental determination of heavy ion irradiation damage was performed on post-irradiation XSEM images using ImageJ software to measure cracking and discoloration penetration depths.

Thermal and vibrational spectra were collected for starting materials, silane-functionalized ceria NPs, and silane-ceria/EPON composites. IR transmission and reflectance spectra were collected on a Bruker Tensor II spectrometer equipped with a Pike GladiATR attenuated total reflectance (ATR) or Pike VeeMAX III automated grazing angle specular reflectance stages. Grazing angle spectra were collected at 30, 50, and 80° angles. A total of 32 scans with 4 cm^{-1} resolution were obtained for each sample. Baseline corrections were performed on the collected spectra and normalized using the peak at 825 cm^{-1} as an internal reference. Thermogravimetric analysis (TGA) was performed under a flowing N_2 atmosphere using a Q500 TGA spectrometer. Samples were heated from room temperature to 700 °C at a rate of 10 °C/minute. Differential scanning calorimetry (DSC) was carried out using a TA Instruments Q200 V24.11 differential scanning calorimeter. Samples were equilibrated to 0 °C, heated to 200 °C at a rate of 5 °C/minute, and then cooled to room temperature at 10 °C/minute. This cycle was repeated twice. The glass transition temperature was determined from second cooling cycle.

3. Results

3.1 SCA-grafted ceria nanoparticles

3.1.1 FTIR The nature of attachments formed between the silane coupling agents and the surface of the as-received ceria NPs was assessed via FTIR spectroscopy. The appearance, position, and intensity of characteristic vibrational modes were used to confirm successful SCA grafting and compare approximate loading values between the two different silanes. Most features in the spectrum of the unfunctionalized (pristine) ceria NPs are caused by cerium-oxygen interactions on the NP surface.[51,54] The pristine ceria NPs spectrum seen in **Figure S1** displays a prominent absorbance band near 720 cm^{-1} that corresponds to the Ce–O stretching vibration, while the band at 1320 cm^{-1} represents Ce–O–Ce stretching. The intensity of the Ce–OH at 1630 and 3400 cm^{-1} stretches can be used to qualitatively assess the availability of surface hydroxyl groups, which serve as the primary binding site for SCAs.[51,54]

Spectra of ceria NPs with MTES and OTES (**Figures S1a–b**, respectively) show the emergence of new peaks that correspond to vibrational modes of the silane coupling agents. Both MTES and OTES-NPs display absorbance bands associated with Ce–O–Si stretching at 530 and 780 cm^{-1}, as well as the anti-symmetric and symmetric Si–O–Si stretches that occur at 1030 and 1120 cm^{-1}, respectively.[63] Bands representing the silane alkyl groups such as the Si–CH$_3$ stretch at 1270 cm^{-1} can also be observed in the spectra for both SCA–NPs samples, although these bands are much more prominent for the OTES-NPs (**Figure S1b**) due to the long OTES alkyl chain. The OTES-NPs spectrum shows symmetric bending and stretching vibrations of methyl groups at 1460 and 2950 cm^{-1} (respectively), while strong methylene anti-symmetric and symmetric stretches can be seen at 2870 and 2920 cm^{-1} (respectively). The hydrophobic effect of these alkyl chains is seen in the reduced intensity of the OH stretch at 3400 cm^{-1}, which was attributed to water molecules adsorbed to the NP surface.[55,64] Overall, these spectral features confirm successful covalent attachment of alkylsilane molecules to the ceria NPs surface. The small peak at 950 cm^{-1} in the MTES-NPs spectrum indicates the presence of unreacted silanol groups. This peak is not seen for the OTES-NPs, which indicates that the OTES SCA was completely grafted to the NP surface groups.[63] A listing of vibrational mode position and intensity can be found in **Table S2**.

3.1.2 TGA was conducted to examine thermal decomposition behavior of the silane-CeO$_2$ NPs in terms of derivative weight change (DWC) and weight loss (WL), which can be used to estimate the amount of silane surface coverage. The thermal behavior at low temperatures can also be used to verify the formation of covalent attachments between the silanes and ceria NPs. Residual or weakly adsorbed silanes are lost between 70–130 °C, while covalently bound silanes are thermally stable up to ~300 °C.[55] As seen in **Figure S2**, the lack of significant weight loss below 300 °C for the SCA–NPs confirms the lack of free silanes and supports the formation of covalent silane attachments to the NPs surface.

The WL curves show three distinct weight loss events for both samples. Weight loss by silane-modified NPs in the low temperature regime results from the loss of water molecules physisorbed to the NPs surface between 100–200 °C.[51] Below 300 °C, the MTES-NPs experienced a slightly greater percent WL (2.2%) as compared to the OTES-NPs (1.8%), which is in agreement with the increased surface water

adsorption observed as the increased intensity of the OH stretch at 3400 cm^{-1} in the MTES–NPs FTIR spectrum. In the 300 – 700 °C region, minor weight losses of 1.0% and 1.4% were observed for the MTES-NPs and OTES-NPs, respectively. Weight loss in this region is associated with degradation of silane hydrocarbon moieties via C–C and Si–C bond cleavage.[55,64] The greater weight loss by OTES, with its long alkyl chain, is in agreement with that phenomenon. At temperatures above 700 °C, weight loss reflects the total decomposition of surface grafter silanes.[51] Both samples experienced the greatest weight loss in this region, with values of 6.6% for MTES-NPs and 12.0% for OTES-NPs. A summary of weight loss data can be found in **Table S3**.

Quantitative evaluation of NP surface coverage by MTES vs. OTES was performed using **Equation 4** to estimate the total weight percent of surface-grafted silane:

(5) $$\text{Grafted silane (\%)} = \frac{p_f - (s_i - s_f)}{p_f}$$

where p_f represents mass of the pristine ceria TGA samples recorded at 900 °C, while s_i and s_f represent the masses of the silane-NPs recorded at 700 and 900 °C, respectively.[54] This equation compares weight loss associated with the decomposition of grafted silanes against the pristine ceria NPs, which show zero weight loss in that region due to their thermal stability and the absence of grafted silanes. The results yielded grafted silane weight percentages of 10% and 16% for MTES and OTES-NPs, respectively. This supports a more thorough coverage of the ceria NPs surfaces by OTES as compared to MTES. which could be attributed to the long OTES alkyl chain enabling a thicker coverage of the NP surface. Previous studies have observed that long SCA alkyl chains promote silanol groups to condense with NP surface hydroxyl groups, whereas the silanol groups of short chain
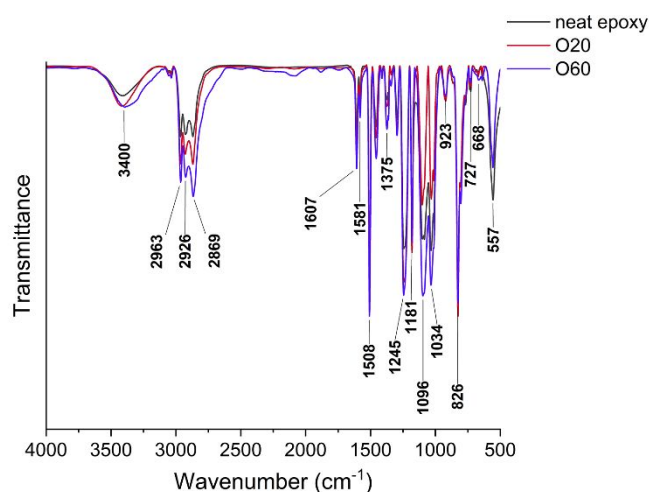

Figure 2. FTIR spectra of neat epoxy compared to low (20 wt%) and high (60 wt%) loading nanocomposites. SCA type did not affect composite surface chemistry.

SCAs tended to bond with reach other to form a cross-linked coating layer around the NPs.[50,64]

The derivative weight change (DWC) curves illustrate distinct differences in thermal behavior between MTES-NPs and OTES-NPs. As seen in the peaks at 150 and 875 °C, the MTES-NPs experienced higher weight loss activity at low temperatures. In contrast, the OTES-NPs show minimal low-temperature activity but far greater weight change at high temperatures (700–900 °C) associated with silane decomposition. This serves as evidence for higher silane surface loadings for OTES-NPs, which was supported through quantitative analysis of weight loss data.

3.2 SCA–NP/EPON nanocomposites

3.2.1 FTIR   FTIR spectra collected for low (20 wt%), high (60 wt%), and neat epoxy samples were compared in order to assess the potential impacts of SCA type and nanofiller loading on the surface chemistry of the materials. As represented by the spectra in **Figure 2**, neither variable had a significant impact on peak position or intensity. Both spectra contain multiple strong peaks associated with aromatic ring vibrational modes, such as the C–H out of plane bending at 668 and 727 cm^{-1}, ring breathing at 923 cm^{-1}, and C=C and C–C stretching at 1508 and 1581 cm^{-1} (respectively).[65–68] The *para*-disubstitution of the benzene rings in the epoxy unit is represented by the ring bending mode at 826 cm^{-1} and C–C stretching at 1606 cm^{-1}.[69] The epoxy unit ether linkages created in the curing reaction give rise to the strong absorbance bands for the alkyl aryl ether R–O–C stretch at 1034 cm^{-1} and C–O–C stretch at 1244 cm^{-1}.[70] The dialkyl ether of the amine unit can be observed as the C–O–C stretching band at 1094 cm^{-1}.

Table 1. Vibrational modes of neat epoxy and nanocomposite samples

$\tilde{v}$ (cm^{-1})	Group	Vibration
3400	Epoxy hydroxyl	O–H v
2960	Methyl	CH$_3$ v
2920	Methylene	CH$_2$ v_s
2870	Methylene	CH$_2$ v_{as}
1606	*p*-disubstituted benzene	C–C v
1581	Aromatic ring	C–C v
1508	Aromatic ring	C=C v
1375	Methyl	CH$_3$ δ
1244	Alkyl aryl ether (epoxy)	C–O–C v
1183	Isopropylidene	C–CH$_3$ v
1094	Dialkyl ether (amine)	C–O–C v
1034	Alkyl aryl ether (epoxy)	R–O–C v
923	Aromatic ring	Ring breathing
826	*p*-disubstituted benzene	Ring δ
727	Aromatic ring	C–H δ_{op} (2 bands)
668	Aromatic ring	C–H δ_{op} (2 bands)
557	Amine unit	C–H and C–N δ

The strong band at 1183 cm^{-1} is associated with C–CH$_3$ stretching by the isopropylidene group on the bisphenol A (BPA) moiety.[70,71] Methylene and methyl group stretches near 2900 cm^{-1} represent alkyl groups in the amine and epoxy units of the crosslinked structure. The OH stretch at

3400 cm^{-1} was attributed to epoxy hydroxyl groups in the composites, with a possible contribution from surface adsorbed water on the SCA–NPs.[69,72] The position and intensity of these peaks form a baseline for comparison with the irradiated samples to determine degradation pathways and the resulting products. **Table 1** lists these peaks.

3.2.2 XEDS XEDS mapping was used to assess the homogeneity of SCA–NPs dispersion throughout the epoxy matrix. **Figure 3** displays the cerium EDS maps for low (20 wt%) and high (60 wt%) loading levels of MTES and OTES-NPs. The M20 sample in **Figure 3a** shows distinct high and low Ce density areas, which represent MTES-NP aggregates within the epoxy. As seen in **Figure 3b**, aggregation of the MTES-NPs increases at 60 wt% loading. In contrast, the Ce density distribution on the O20 XEDS map (**Figure 3c**) indicates a homogeneous OTES-NP dispersion that is maintained for the high loading O60 sample (**Figure 3d**). This suggests that OTES SCAs more effectively facilitate interactions NP interactions with the polymer matrix when
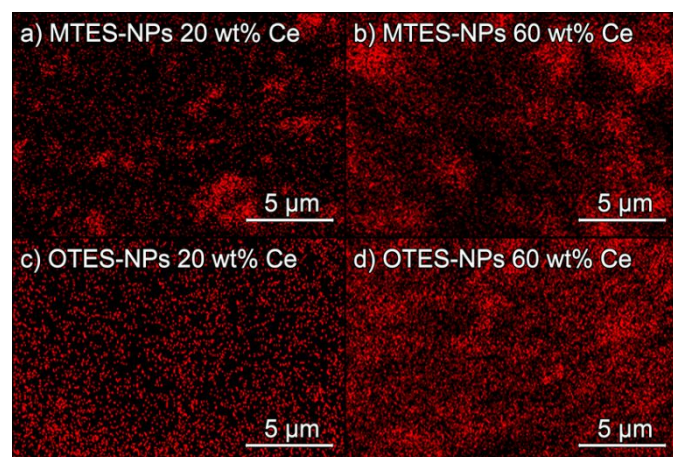

Figure 3. Cerium XEDS maps recorded for nanocomposites containing ceria NPs functionalized by MTES or OTES SCAs at low and high loading levels. (a) MTES, 20 wt%; (b) MTES, 60 wt%; (c) OTES, 20 wt%; (d) OTES, 60 wt%.
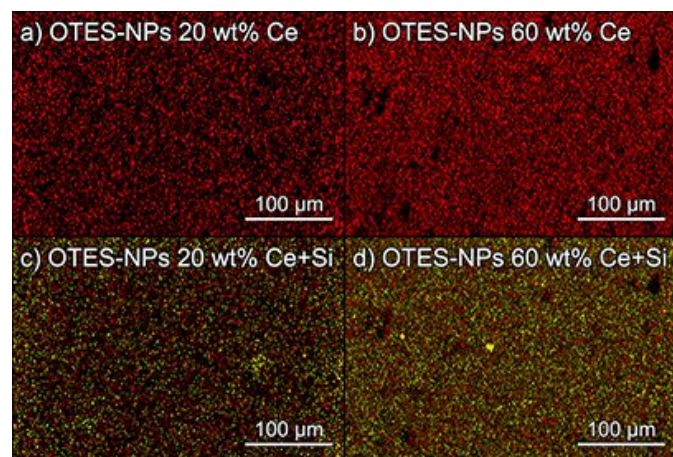

Figure 4. Homogeneous NP dispersion was observed in XEDS maps recorded at lower magnification OTES–NPs nanocomposites. XEDS maps of cerium are shown for (a) 20 wt% and (b) 60 wt% OTES–NPs loading. Figures (c) and (d) show maps of the same samples that include silicon as well as cerium to represent surface-grafted OTES SCAs.

compared to MTES. To confirm the formation of homogeneous OTES-NP dispersions for low and high loading

levels, Ce and Si XEDS maps were recorded at lower magnification. The maps shown in **Figure 4** indicate that dispersion homogeneity was achieved for both loading levels, verifying that dispersion quality was not affected by increased loading levels of OTES-NPs.

3.2.3 TGA Thermal analysis via TGA was conducted on the as-synthesized MTES and OTES composites to assess possible changes in thermal decomposition behavior due to the presence of silane-NPs at different loading levels. **Figure 5** displays the weight loss curves collected from TGA analysis of SCA–NPs with low and high loading levels. Analysis of these data indicated a two-step thermal decomposition process with an initial weight loss in the low-temperature regime (below 300 °C) attributed to water elimination resulting from unsaturated C–C bond formation. This was followed by the main decomposition process, which occurred between 300–700 °C and represents chemical bond degradation within the epoxy networks.[3] The residual material consists of carbonaceous decomposition products from epoxy degradation and thermally stable ceria NPs.
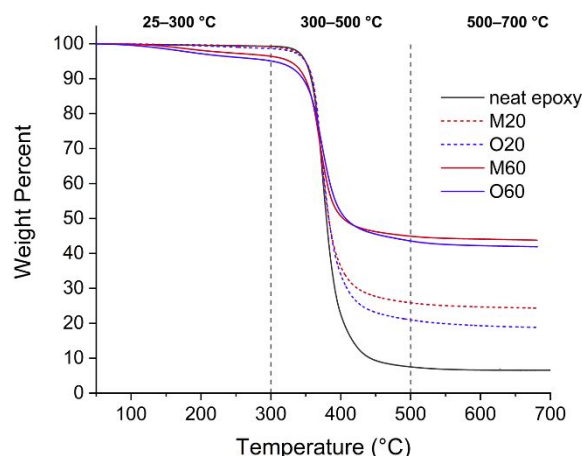

Figure 5. TGA weight loss curves for neat epoxy and composites with low (20 wt%) and high (60 wt%) nanofiller loading.

The derivative weight change (DWC) curves were analyzed with respect to the temperature and rate of the decomposition maximum (DWC$_{max}$). The DWC$_{max}$ temperature was found to be 374 °C for all composite samples regardless of loading or silane functionalization, but represented a ~4 °C decrease over the neat epoxy (**Table S4**). Decomposition rates recorded at the DWC$_{max}$ temperature of 374 °C showed a consistent decrease with increased nanoparticle loading, with no significant difference observed between MTES and OTES samples. These rate decreases are consistent with the reduction in overall weight loss by the MTES and OTES composites relative to the neat epoxy, as described above. DWC curves can be found in **Figure S3**.

3.2.4 DSC DSC thermograms of the pre-irradiated composites were used to determine if differences in silane functionalization or NPs loading had any effects on the glass transition temperature (T$_g$). **Table S5** lists the T$_g$ values for

the EPON blank and MTES and OTES composites over a range of nanoparticle loadings. For all composite samples, T_g was lower relative to the neat epoxy. Composites with low loading (20%) showed a minimal T_g decrease, with the composite samples displaying a general trend of decreasing T_g with increasing NPs loading. The highest loading samples showed a T_g decrease of 13.1 and 6.7 °C for MTES and OTES composites, respectively. A graphical summary of T_g curves for each loading value of MTES and OTES composites is shown in **Figure S4.**

Nanofillers are often added to polymers to enhance the thermal and mechanical stability of the composite, and studies commonly report an increase in T_g for nanofiller-loaded composites over the neat polymers. However, T_g depression is also widely reported for nanocomposites, and several different explanations are offered for the phenomenon.[73] One theory involves the creation of extra free volume by the increased NP/matrix interfacial interaction area, thereby enhancing polymer segment mobility.[47,74,75] A second explanation relates to nanofiller impacts on the crosslink density of the epoxy matrix. Multiple studies have observed that T_g continues to drop as nanofiller loading levels increase.[76,77] This behavior is attributed reduced crosslinking in the epoxy matrix caused by nanofillers, which dramatically alter the viscosity and undergo chemical interactions with the polymer.

Another potential explanation for T_g depression is non-uniformity of NP dispersion throughout the composite due to NP agglomeration, a well known factor behind decreased mechanical and thermal stability that is most severe when nanofillers lack silane or other surface modifications.[78,79] The agglomeration of unmodified NPs is driven by their incompatibility with the polymer matrix due to the NPs high surface energies,[51] strong interparticle van der Waals interactions,[80] and hydrophobicity mismatch.[81] This commonly produces microscale aggregates with numerous air gaps or voids between the clusters that act as physical defects in the composite.[80–82] These void-filled agglomerates hinder effective interfacial interaction, disrupt epoxy networks, and decrease crosslinking density to cause T_g depression.[80]

The DSC results for MTES and OTES composites suggest that each of the factors above could have an impact on T_g behavior (**Table S5**). A T_g depression relative to the neat epoxy was observed for all composites, which likely represents some enhancement of polymer segment mobility by the extra free volume at abundant NP interfaces. However, the very small value of the T_g depression (~1–2 °C at 20 wt%) suggests that polymer mobility has a minimal impact compared to other factors. In contrast, a clear trend is observed in T_g depression as a function of nanofiller loading level. Both OTES and MTES composites showed a consistent, direct relationship between nanofiller loading and T_g depression. This is most likely attributed to disruptions in epoxy resin crosslinking, which grow more severe as nanofiller loading increases.

A distinct difference between the behavior of OTES and MTES composites is observed when examining T_g depression vs. nanofiller loading level. While the 60 wt% samples of both composites had the lowest T_g, the overall T_g decrease was much greater for MTES (13.1 °C) than for OTES (6.7 °C) (**Table S5**). This most likely results from a significant increase in the formation of agglomerates from MTES-NPs. As seen in **Figure 4**, EDS results confirm that the OTES-NPs were homogeneously dispersed throughout the epoxy matrix at both low and high loadings. The MTES-NPs formed a less homogeneous dispersion, with both low and high loading samples showing distinct areas of agglomeration (**Figure 5**). These T_g results are consistent with the known effects of agglomerates, which act as void-filled defects within the epoxy matrix. This also supports that OTES functionalized NPs had improved dispersion relative to MTES.[74]

3.3 Neat epoxy and composite samples after heavy ion irradiation

Characterization via FTIR, surface SEM, and XSEM was conducted for the neat epoxy and the 20 and 60 wt% samples of both MTES and OTES-capped ceria nanofillers. Due to the superior homogeneity of the OTES-NPs dispersion in the
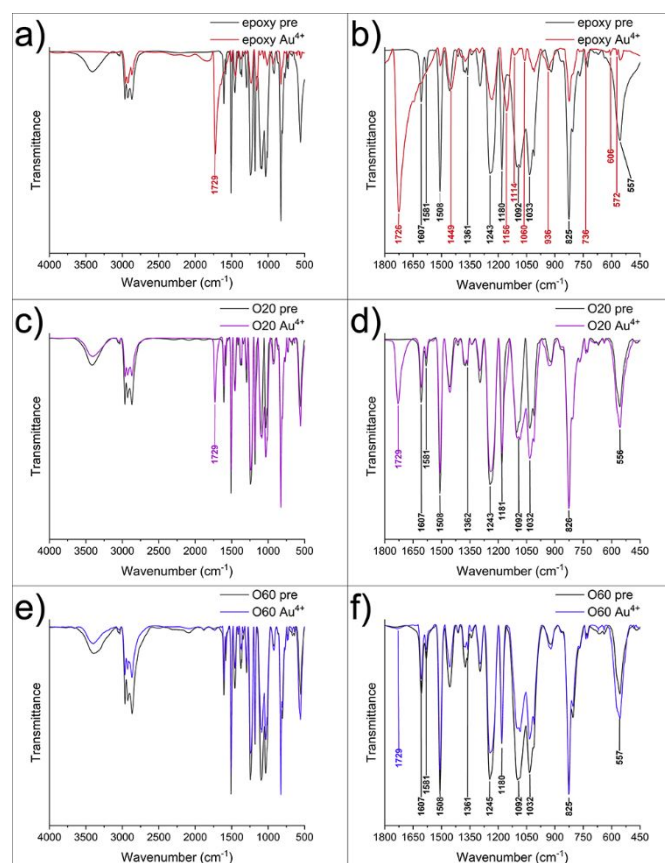

Figure 6. FTIR spectra recorded before and after irradiation of (a–b) neat epoxy; (c–d) O20; and (e–f) O60 samples.

epoxy matrix, results and discussion are presented for the

irradiated epoxy, O20, and O60 samples only. Data for MTES can be found in the supporting information.

3.3.1 FTIR **Figure 6** shows FTIR spectra collected for the neat epoxy and O60 samples before and after heavy ion irradiation. The neat epoxy sample (**Figure 6a–b**) showed extensive spectral changes after irradiation, including a significant reduction in overall intensity, the absence of multiple prominent peaks from the pre-irradiation spectrum, and the emergence of seven strong absorbance bands below 1800 cm^{-1}. Disappearance of the hydroxyl stretch at 3400 cm^{-1} is associated with the irradiation induced degradation of the epoxy aromatic character via dehydration of secondary alcohols to form double bonds or the conversion of the hydroxyl groups to carbonyl products.[65–67] Alteration of the O20 and O60 spectra occurred to a much lesser extent (**Figure 6c–f**), and was observed as a general, less significant reduction in intensity with no absent peaks. Spectra of the irradiated O20 and O60 samples were similar except for the emergence of a strong absorbance band at 1729 cm^{-1} for O20.

The FTIR results confirm carbonization of the irradiated sample surfaces by the decreased intensity of vibrations associated with methyl groups and ether linkages, which indicates the debonding of weak groups to form a stable carbonaceous structure via radical reactions.[30,72,83] Depolymerization of polymer chains, which results from thermal energy generated by radiolytic processes, is known to contribute to the formation of a primary carbonaceous char layer on the surface of irradiated epoxy matrix composites.[84–86] Degradation of epoxy aromatic groups by radical attack can also contribute to surface carbonization due to the formation of highly conjugated products.[65,83]

3.3.2 Visual and SEM examination Drastic changes to all samples after heavy ion irradiation were evident from visual inspection, with detailed damage analysis conducted via surface and cross-sectional SEM imaging. Visual inspection revealed that irradiated samples displayed visible
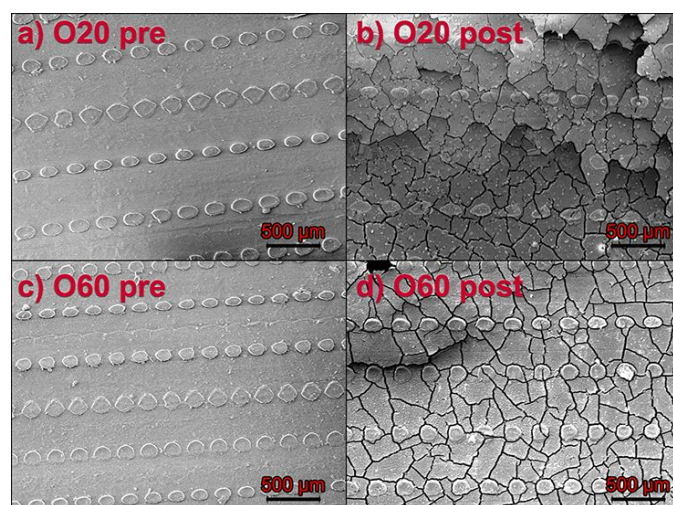

Figure 7. Surface SEM micrographs recorded for O20 and O60 samples recorded before and after heavy ion irradiation.

cracking and heavy surface discoloration from light tan to

black. Comparison of surface SEM micrographs collected before and after irradiation confirms extensive irradiation induced surface changes via widespread crazing, blistering, and shearing (**Figure 7**). While the unirradiated O20 and O60 samples) showed very similar smooth surfaces featuring lines of raised ovals (an artifact of the 3D-printed epoxy mold), a much greater extent of delamination was observed in the low loading sample after irradiation (**Figure 7b**). Surface SEM images for the MTES composites are shown in **Figure S5**.
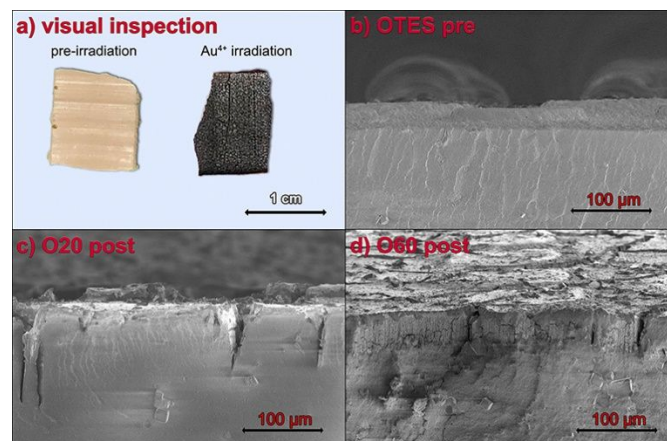

Figure 8. (a) Visual inspection of O60 samples before and after heavy ion irradiation. XSEM images comparing OTES samples before irradiation (b) to irradiated (c) O20 and (d) O60 samples.

XSEM imaging revealed significant changes in the irradiated samples and confirmed the extension of surface damage into the composite interiors. The XSEM micrographs shown in **Figure 8** demonstrate the formation of a distinct damage layer in the irradiated samples that is defined by cracking, shearing, and discoloration. Comparison of the low and high loading samples shows a trend similar to the surface SEM results, with the unirradiated samples showing few differences but more extensive damage emerging in the O20 sample after irradiation (**Figure 8c**). Depth measurements of the modification layer were taken from multiple XSEM micrographs of each irradiated sample (**Table 2**). These measurements indicate that discoloration extended an average of 9.39 µm from the O20 surface, with maximum penetration extending to 17.1 µm. These values were greater than the corresponding measurements of 7.17 µm (average) and 11.3 µm (maximum) that were recorded for the O60 sample. XSEM images for the OTES composites are shown in **Figure S6**.

Table 2. Damage measurements from XSEM images.

Penetration Depth (µm)	M20	O20	M60	O60
Discoloration, mean	12.6	9.39	9.25	7.17
Discoloration, max	17.2	17.1	15.4	11.3
Cracking	77.4	73.6	45.8	28.7

XSEM imaging was also used to examine the influence of nanofiller loading on matrix cracking phenomena, which first appear on the composite surface and then propagate throughout the matrix. Encountering the nanofiller changes the original propagation path of the crack and produces numerous smaller cracks. These small cracks absorb and consume energy from the original, effectively mitigating further cracking damage.[87] Observed cracking penetration depths followed the expected trend, extending to 73.6 μm in O20 and 28.7 μm in O60. As shown in **Table 2**, all measurements show a greater extent of damage onto the top surface in both the M20 and M60 samples compared to O20 and O60. Increased damage incursion would be expected for materials in which NPs interact poorly with the polymer matrix and settle to the bottom of the sample (as indicated by the TGA results). The reduced damage penetration in the OTES samples supports the importance of dispersion homogeneity in mitigating irradiation damage.

3.3.3 SRIM simulation results SRIM estimations of ion penetration range and vacancy production for neat epoxy, 20 nanofiller wt% ("Ce20"), and 60 nanofiller wt% ("Ce60") samples are listed in **Table 3**. It should be noted that while SRIM simulations provide valuable information on cumulative atomic displacements that can lead to unpredictable irradiation induced microstructural evolution, their accuracy is limited by programmatic assumptions about the target material structure and composition. These assumptions include an amorphous target material structure and homogeneous chemical distribution, which reduce their effectiveness for use with nanocomposite materials. The assumptions also do not account for the nanoscale impact of the filler, surface functionality, or how well the nanofiller is distributed.

The range results in **Table 3** express 20 MeV Au penetration in terms of total depth and the distribution of Au ions implanted throughout the target. Values for average 20 MeV Au ion penetration depth show a distinct decrease from the neat epoxy (7.3 μm) to Ce20 (3.8 μm) and finally Ce60 samples (2.4 μm). The same trend is observed for the maximum Au ion penetration depth, which decreased from 8.8 μm (neat epoxy) to 5.0 μm (20 wt%) to the lowest value of 3.1 μm (wt%). These data show a clear relationship between higher nanofiller loading levels and reduced Au penetration into the target.
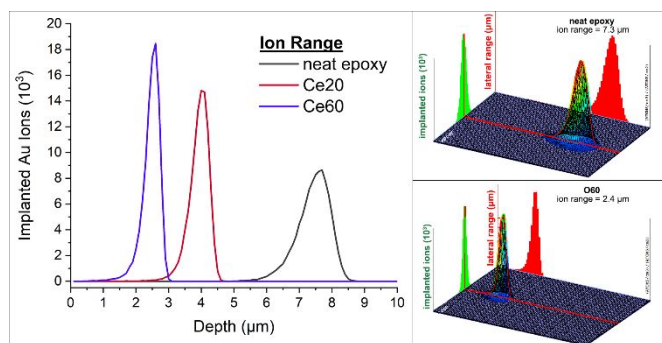

Figure 9. Summary of implanted ion range results from SRIM simulations with 3D images of range for neat epoxy and O60 samples.

Figure 9 shows a plot of implanted ion concentration as a function of depth for each sample, with each curve representing the distribution of 50,000 Au ions within the target material. The Ce60 curve demonstrates that implantation of 20 MeV Au ions was confined to a very shallow distance from the sample surface. In contrast, the neat epoxy curve shows Au implantation spread over a greater range to an increased depth, extending the damage area further throughout the sample.

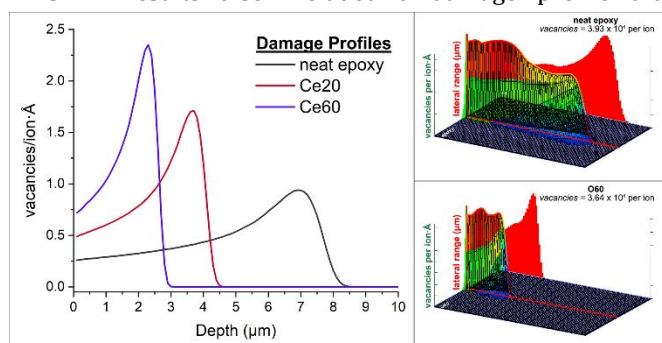SRIM results also included a damage profile that

Figure 10. Damage profile (vacancy production) results from SRIM simulations with 3D images of damage profiles for neat epoxy and O60 samples.

represents total damage events as vacancies created through displacement of target atoms by collisions with incident Au. As seen in **Table 3**, values for both average vacancies produced per Å·ion and total vacancies per ion decreased significantly as nanofiller loading increased from zero to 60 wt%. The increase in maximum vacancies per Å·ion is due to the confinement of vacancy production within a narrow depth range for Ce60, as opposed to the wider distribution over an increased depth range in the neat epoxy. These trends are shown by the damage profile plot (**Figure 10**).

4. Discussion

Table 3. SRIM simulation results.

|	Neat epoxy	Ce20	Ce60
Range (μm)			
Average	7.3	3.8	2.4
Maximum	8.8	5.0	3.1
Vacancy production (vacancies Å^{-1}·ion^{-1})			
Average	0.393	0.389	0.365
Maximum	0.939	1.71	2.35
Total per ion (10^3)	39.35	38.93	36.54

The general pathway of interaction between heavy ion beams and polymeric materials proceeds via generation of highly excited ionic and radical species, which incite crosslinking and chain scission reactions that modify the surrounding material.[24,88,89] While prior studies of amine crosslinked epoxy resins tended to classify either crosslinking or chain scission as the predominant degradation mechanism, more recent research has concluded that both processes can occur simultaneously or in sequence.[24,33,34,83] Reaction selectivity is determined by multiple factors such as irradiation conditions and epoxy-amine network structure, making it difficult to identify the dominant process.[34,90]

For example, the presence of active sites and defects is known to cause formation of side chains and end groups via chain scission.[34] Chain scission is also associated with aliphatic amine units, which are highly susceptible to radical attack.[24] Crosslinking has been found to occur between diphenyl groups in adjacent molecules via pendant methyl groups,[66] between radicals at alpha positions to heteroatoms in the amine moiety,[91] and within networks with aromatic amine crosslinkers.[92] The presence of oxygen causes alkyl radicals to terminate via coupling to cause crosslinking, while they undergo disproportionation to form unsaturated carbon bonds under vacuum.[91,93] Further, differentiating between chain scission vs. crosslinking processes becomes irrelevant past a certain accumulated dose level. Continuing dose accumulation will eventually cross the threshold for irreversible degradation processes to cause critical damage to the material.

In this study, we examined the impact of adding ceramic nanofillers at various loading levels on damage propagation routes and suppression under heavy ion irradiation. A mechanistic examination of known degradation pathways for epoxy resins was conducted to determine if the nanofillers altered or prevented scission of certain bonds. We also investigated the potential mechanistic influence of ceria nanofillers, which can enhance polymer irradiation resistance via radical trapping or absorbing implanted energy from the epoxy matrix.[41,44] Three main pathways were identified based on literature, which indicated that radiolytic degradation in amine-crosslinked epoxy materials proceeds primarily via bond scission at susceptible sites within the polymer network.[94,95] While these mechanisms are presented as the result of bond scission, the presence of crosslinking phenomena is also suspected. Bond scission can even be seen as a contributor to crosslinking, as it generates radicals that recombine with nearby polymer chains to effectively crosslink the polymer.[28] Determination of the primary mechanisms was supported by identification of degradation products in the post-irradiation FTIR spectra.

4.1 Potential degradation pathways in amine-crosslinked epoxy materials

Scheme 2 illustrates the three major vulnerable areas in the amine-crosslinked epoxy network, with carbon bond
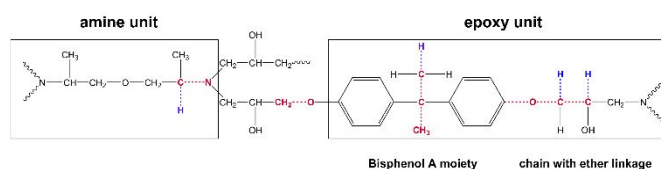
Scheme 2. Potential sites for hydrogen abstraction (blue) and C–C, C–N, or C–O bond cleavage (red) in each unit of the amine crosslinked epoxy network.

cleavage sites indicated in red and hydrogen abstraction sites in blue.[1,67,83,94,95] These three areas include the amine aliphatic segment, the methyl groups of the bisphenol A (BPA) moiety, and the ether linkage and the carbon with the hydroxyl group in the aliphatic epoxy segment.[83]

4.1.1 Amine aliphatic hydrocarbon segment As seen in **Scheme 3**, degradation of the amine unit proceeds via radiolytic hydrogen abstraction and radical formation, followed by β scission of the $C^\bullet$–N bond to generate an allyl amine as the main product.[92] Subsequent hydrogen abstraction from the unreacted polymer ("PH") by the amine radical can generate a secondary amine product.

4.1.2 Epoxy aliphatic segment Weak points in the epoxy aliphatic segment occur at carbon atoms that suffer destabilizing effects from their linkage to highly electronegative O and N atoms, such as the carbons in the ether linkage and the tertiary alcohol.[95] **Scheme S1** shows radical initiation via direct radiolytic hydrogen abstraction from the hydroxyl-functionalized carbon (C_b) to form alkyl Radical B ($C_b^\bullet$) and a radical hydrogen, which abstracts another hydrogen from the unreacted polymer (PH) to generate molecular hydrogen and an alkyl radical ($P^\bullet$). $C_b^\bullet$ can undergo intermolecular hydrogen transfer to generate Radicals A and C. **Scheme 4** shows two potential degradation routes for $C_a^\bullet$ and $C_b^\bullet$. The $C_a^\bullet$ mechanism proceeds via radical beta scission of the ether bond, generating a phenoxy and a $C_a^\bullet$ chain radical, which induces chain scission and hydrogen abstraction of the unmodified polymer (PH) to generate BPA as a final product. The $C_b^\bullet$ mechanism proceeds via rearrangement and disproportionation to generate an alkyl-substituted ketone.[95]

4.1.3 BPA moiety Radiolytic degradation in the bisphenol A moiety centers on the methyl groups, one of which is removed by direct radiolytic chain scission to form Radical J (**Scheme S2**).[94] The radical chain mechanism of Radical J has multiple potential pathways, which are shown in **Scheme 5**. The first involves radical recombination to form diphenyl vinylidene. Radical J can also react with PH via β scission at the $J^\bullet$–methyl bond to form diphenyl methylene or at the $J^\bullet$–phenol bond to a methyl phenol radical. Diphenyl methylene can go on to react with PH via β scission to form methylene diphenol (bisphenol F), while the methyl phenol radical can terminate via hydrogen abstraction to generate methyl phenol or via disproportionation to give phenyl formate. **Scheme S3** shows an alternative pathway for BPA moiety degradation

via Radical K, which undergoes isomerization to form an aromatic ketone.

## 4.2 Elucidation of damage mechanisms using vibrational data

Epoxy degradation is readily observed via FTIR as changes in absorbance band position and intensity.[96] Previous studies have established that under sufficiently energetic irradiation, the intensities of all absorbance bands are expected to decrease relative to their pre-irradiation
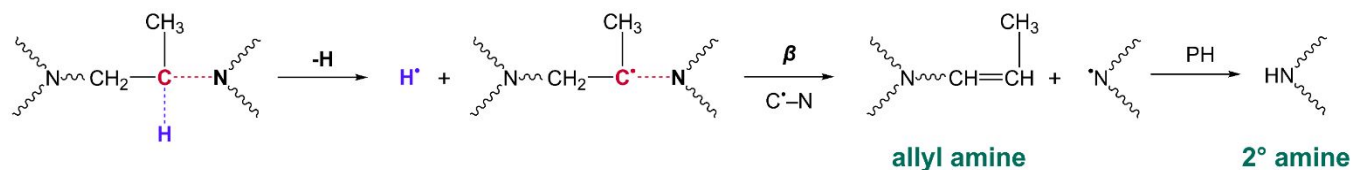
Scheme 3. Degradation of the amine aliphatic segment.
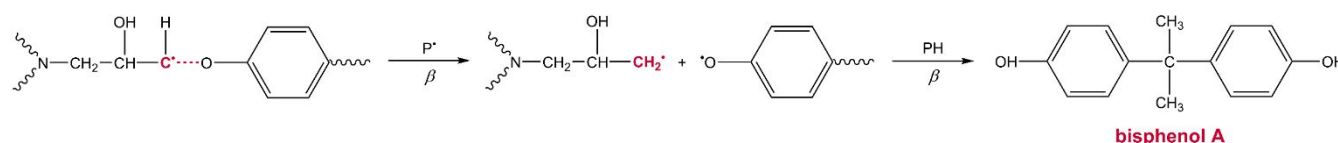
Scheme 4. Two pathways for radical driven degradation of the epoxy aliphatic segment via radiolytic hydrogen abstraction from the carbon alpha to the ether linkage (C_a) or the carbon attached to the hydroxyl group (C_b).
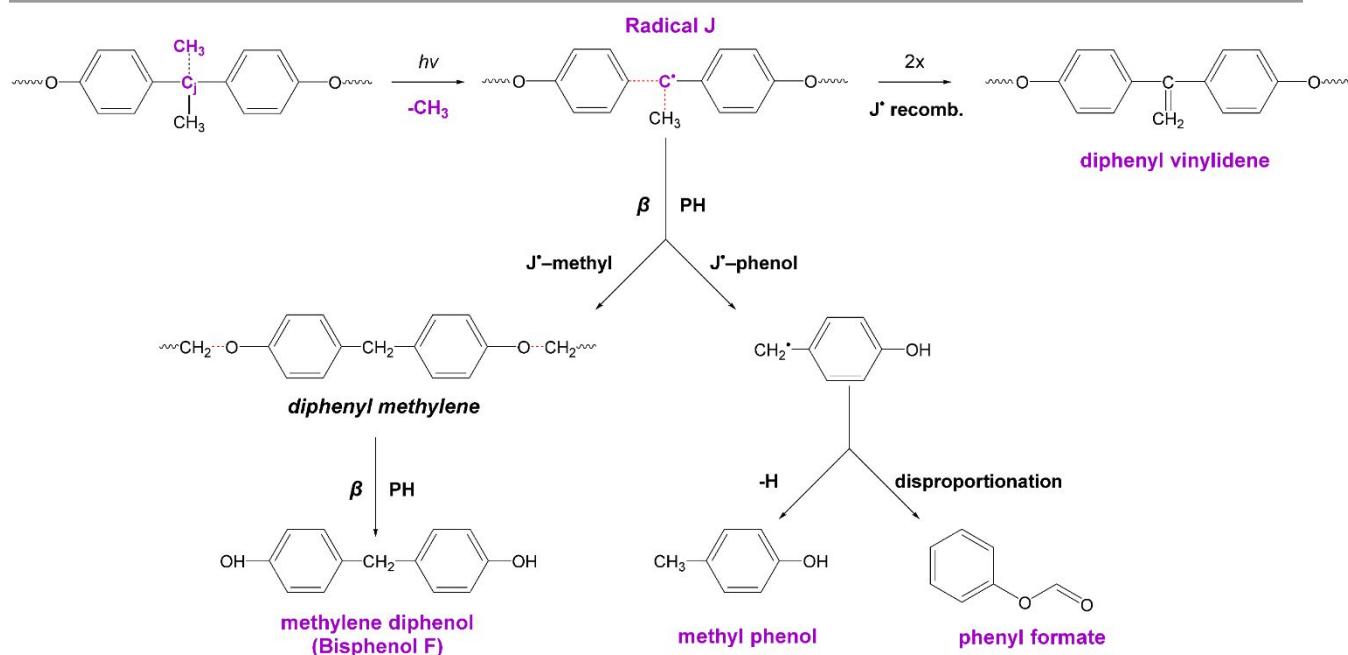
Scheme 5. Multiple reaction pathways for Radical J causing degradation of BPA moiety, including radical recombination to form vinylidene species, and chain scission routes leading to phenol and ketone products.

values.[97] In addition, new bands are expected to emerge representing the formation of new chemical species from bond cleavage, reformation, and the release of hydrogen and other volatile organic compounds as a result of irradiation.[20] Irradiation-induced changes to the polymer chemical structure may also produce a carbonaceous material with properties similar to hydrogenated amorphous carbon,

which is often observed as the formation of conjugated carbon bonds.[96]

4.2.1 Neat epoxy   The post-irradiation FTIR spectrum of the neat epoxy displayed far more extensive changes in peak presence, intensity, and position compared to the composite samples. **Figure 6a–b** shows these changes,

Table 4. Vibrational modes of neat epoxy and composites after heavy ion irradiation. Bold text indicates appearance after heavy ion irradiation.

$\tilde{v}$ (cm^{-1})	Group	Vibration
3400	Epoxy OH	O–H v
1726	**Alkyl-substituted ketone**	**C=O v**
1607	*p*-disubstituted benzene	C–C v
1581	Aromatic ring	C–C v
1508	Aromatic ring	C=C v
1449	**Vinylidene**	**CH$_2$ δ_s**
1361	Methyl	CH$_3$ δ
1243	Alkyl aryl ether (epoxy)	C–O–C v
1180	Isopropylidene	C–CH$_3$ v
1154	**Phenol**	**C–O v**
1116	**Phenyl formate**	**C–O v**
1092	Dialkyl ether (amine)	C–O–C v
1060	**Vinylidene**	**C–H δ**
1033	Alkyl aryl ether (epoxy)	R–O–C v
937	**Allyl amine**	**CH$_2$ δ**
826	*p*-disubstituted benzene	Ring δ
736	**Secondary alkyl amine**	**N–H v**
571	**Phenol**	**Ar–OH v**
557	Amine unit	C–H and C–N δ

which were primarily observed below 1800 cm^{-1}, as peaks that are absent or greatly reduced in intensity from the pre-irradiation spectrum (marked in black) and peaks that emerged after irradiation (marked in red). These peaks were identified based on the mechanisms described above and are listed in **Table 4**. Among the peaks that were reduced or eliminated after irradiation were many associated with the aromatic character of the target material, particularly a loss in the *para*-disubstitution of the phenoxy groups represented by the ring bending and C–C stretching vibrations at 826 and 1607 cm^{-1} (respectively). The loss of aromatic character is further supported by the drastic reduction and disappearance of aromatic ring C–C and C=C stretching vibrations at 1581 and 1508 cm^{-1}, respectively. Degradation of the epoxy aliphatic segment via cleavage of the ester linkage (**Scheme 4**) is supported by the reduced intensities of the alkyl aryl ether R–O–C and C–O–C stretches at 1033 and 1243 cm^{-1} (respectively). Extensive degradation of the BPA moiety via radical chain reactions (**Scheme 5**) is suggested by the disappearance of the isopropylidene C–CH$_3$ stretch at 1180 cm^{-1} and the methyl bend at 1361 cm^{-1}. Amine unit degradation is indicated by the disappearance of the dialkyl ether C–O–C stretch at 1092 cm^{-1}.

Analysis of the vibrational modes emerging after irradiation enabled the construction of a more complete overall degradation scheme when coupled with the identifications described above. The new absorbance bands at 736 and 936 cm^{-1} were attributed secondary alkyl amine N–H and allyl amine CH$_2$ bending modes associated with the products of amine unit degradation (**Scheme 3**). Emergence of the strong peak at 1726 cm^{-1} was found to represent the carbonyl C=O stretch of an alkyl-substituted ketone generated by β scission of the ether linkage in the epoxy aliphatic segment, followed by radical rearrangement and disproportionation (**Scheme 4**). The disappearance of the hydroxy stretch at 3400 cm^{-1} in the irradiated neat epoxy spectrum was assigned to the dehydration of epoxy segment alcohols to generate the carbonyl products.

The remaining new absorbance bands, which constituted the majority of post-irradiation peaks, were associated with the products of BPA moiety degradation via reaction pathways of Radical J (**Scheme 5**). These include the phenol aromatic ("Ar") Ar–OH and C–O stretches at 571 and 1154 cm^{-1} (respectively), the phenyl formate C–O stretch at 1116 cm^{-1}, and the vinylidene N–H and CH$_2$ bends at 1060 and 1449 cm^{-1} (respectively). Each of the potential Radical J reactions were represented by these products, although methyl group scission and radical recombination seem to be prominent pathways based on the number and intensity of associated degradation products in the FTIR spectra.

4.2.2 Composites   Overall, the occurrence of surface carbonization and the disappearance of FTIR vibrational modes for susceptible methyl and ether groups from the neat epoxy spectrum are in agreement with previously reported degradation pathways in which radical driven debonding is initiated by the ionization and displacement effects of incident HZE ions.[24,68,87,93] The beneficial impacts of SCA–ceria nanofillers are evident from XSEM imaging and the dramatic difference between the post-irradiation FTIR spectra of the neat epoxy vs. the composites. The FTIR spectra for irradiated O20 and O60 samples are shown in **Figure 6c–f**, with both displaying fewer spectral changes than the neat epoxy.

The major difference between the irradiated O20 and O60 spectra was the emergence of a strong absorbance band at 1729 cm^{-1} in the O20 sample (**Figure 6c–d**). As in the neat epoxy, this vibration was assigned to the C=O stretching of an alkyl substituted ketone, which arises from cleavage of the ether linkage in the epoxy aliphatic segment. The absence of a carbonyl band in O60 indicates that this degradation pathway is suppressed by high concentrations of homogeneously dispersed SCA–ceria nanofillers within the epoxy matrix. These results indicate that the SCA–ceria nanofillers effectively reduced ion penetration depth and prevented much of the damage accumulation that was incurred by the neat epoxy sample.

4.2.3 Summary of damage processes   Based on the results of vibrational analysis, it was concluded that degradation of the sample materials under heavy ion irradiation proceeded via radiolytic radical chain scission, with damage concentrated in methyl groups of the BPA

moiety. Radical driven reactions also caused the cleavage of C–O and C–N bonds in the epoxy and amine units of the amine-crosslinked epoxy network. Based on the observed differences in damage between the neat epoxy and composite samples, it was concluded that the nanofillers functioned as barriers to radiation damage through two main processes. The first involves the nanofillers absorbance of energy released by HZE ions, diverting energy transfer away from the polymer backbone and subsequently preventing thermal depolymerization.[23,37,38] The second process involves radical scavenging by the SCA–NPs that is driven by the ceria oxygen buffering process to enhance radical trapping efficiency and prevent the propagation of radical degradation.[31,41] Both processes are closely related to the interfacial interaction areas between the ceria NP surfaces and the surrounding polymer. High loading values of homogeneously dispersed SCA–ceria NPs would maximize the concentration of these interfaces, optimizing nanofiller effectiveness as a barrier to irradiation damage in the composite.

Experimental observations support the effectiveness of SCA–ceria NPs as damage barriers. The irradiation induced degradation processes resulted in mechanical cracking and formation of a discoloration layer, which were observed under SEM. Cracking and discoloration can extend below predicted ion penetration depth due to damage propagation. The reduction in damage penetration depth for O60 vs. O20 samples (**Figure 9**) and suppression of carbonyl formation via epoxy unit degradation by O60 (**Figure 6e–f**) supports the hypothesis that higher loadings of ceria NPs reduce irradiation degradation by providing abundant interfacial surface area that prevents damage processes and accumulation.[3,53,98,99] The XEDS (**Figure 3**) and XSEM results (**Table 2**) support the hypothesis that NP dispersion homogeneity plays an important role in mitigating damage in nanocomposites by maximizing interfacial interaction throughout the nanocomposite volume, which assists in the reduction of damage accumulation.[100,101]

5. Conclusions

Overall, the results of this study strongly support the conclusions that SCA–ceria nanofillers reduce damage area in polymer nanocomposites, and that nanofiller loading and homogeneity of dispersion are key to effective damage prevention. Thermal analysis and electron microscopy revealed differences in composite behavior based on both SCA type and loading level. Cross-sectional EDS (XEDS) mapping of composites loaded with MTES-modified NPs revealed widespread formation of particle agglomerates that increased in size and concentration at higher loading levels. In contrast, XEDS maps of OTES–NPs composites showed homogeneous NP dispersion that was unaffected by nanofiller loading level. DSC results showed that T_g depression by the M60 composites was nearly double that of

O60, which is consistent with the expected impact of nanofiller dispersion homogeneity.

In combination with the SEM/XSEM imaging and SRIM simulation results, the vibrational study confirms that higher nanofiller concentrations significantly increase their effectiveness as barriers to irradiation damage. This is attributed to the absorption of both energy and damage-propagating species through detailed interfacial interactions with the nanofiller surface. These interactions reduce the propagation of thermal and radical-driven degradation processes throughout the polymer matrix. Damage reduction at NP interfaces was concluded to be strongly affected by homogeneous particle dispersion, as well-dispersed nanofillers provide ample energy transfer and radical trapping sites throughout the entire polymer matrix.

The results of this study represent a significant pathway for engineered irradiation tolerance in a diverse array of polymer nanocomposite materials. The use of SCAs with long alkyl chains was found to significantly improve interactions between the nanofiller and polymer matrix, preventing the formulation of NP agglomerates. The use of ceria nanofillers may have further increased the efficiency of radical trapping and scavenging. The fabrication and analysis methods described in this work are highly versatile for adaptation to numerous nanofiller and matrix materials, with applications ranging from space exploration and commercial nuclear energy production to remediation of soil contamination and production of green hydrogen fuel from photocatalytic water splitting. Numerous areas of materials science can benefit from developing the reproducible, effective method described in this work to extend the reliability of polymer materials.

Future work will involve demonstrating how tailoring polymer/ceramic nanofiller interfacial interactions could help to further develop radiation tolerant polymers. This could involve altering nanofiller size, composition, surface chemistry, loading levels and dispersion, and the type of bonding between the nanofillers and the polymer matrix. Substituting the aliphatic Jeffamine T403® crosslinking agent with an aromatic amine may also impact irradiation tolerance. Further mechanistic exploration could involve the use of computational modeling methods such as MD simulations, which require a much higher computational cost but can account for crystalline structures and heterogeneous elemental distribution in order to generate more accurate results for nanocomposite materials.

Funding Statement

Engineering Solutions of Sandia, LLC, a wholly owned subsidiary of Honeywell International, Inc., for the U.S. DOE's National Nuclear Security Administration under contract DE-NA-0003525. The views expressed in the article do not necessarily represent the views of the U.S. DOE or the United States Government.

Author Contributions

Conceptualization, C.D.W.C., E.M.R., L.J.T.; writing—original draft preparation, C.D.W.C.; investigation—C.D.W.C., M.A.R., E.M.R., A.G.B., A.S.P., K.H.; data curation—C.D.W.C., M.A.R., A.G.B., A.S.P.; writing—review and editing, C.D.W.C., E.M.R., K.H., L.J.T.; funding acquisition—E.M.R., K.H., L.J.T. All authors have read and agreed to the published version of the manuscript.

Conflicts of Interest

There are no conflicts of interest to declare.

Acknowledgements

References

1   J. Davenas, I. Stevenson, N. Celette, S. Cambon, J. L. Gardette, A. Rivaton and L. Vignoud, Stability of polymers under ionising radiation: The many faces of radiation interactions with polymers, *Nucl. Instrum. Methods Phys. Res. Sect. B Beam Interact. Mater. At.*, 2002, **191**, 653–661.

2   R. J. Parrish, D. C. Bufford, D. M. Frazer, C. A. Taylor, J. Gutierrez-Kolar, D. L. Buller, B. L. Boyce and K. Hattar, Exploring Coupled Extreme Environments via In-situ Transmission Electron Microscopy, *Microsc. Today*, 2021, **29**, 28–34.

3   Z. Wu, S. Li, M. Liu, Z. Wang and X. Liu, Liquid oxygen compatible epoxy resin: modification and characterization, *RSC Adv.*, 2015, **5**, 11325–11333.

4   U. H. Hossain and W. Ensinger, Experimental simulation of radiation damage of polymers in space applications by cosmic-ray-type high energy heavy ions and the resulting changes in optical properties, *Nucl. Instrum. Methods Phys. Res. Sect. B Beam Interact. Mater. At.*, 2015, **365**, 230–234.

5   K. I. Winey and R. A. Vaia, Polymer Nanocomposites, *MRS Bull.*, 2007, **32**, 314–322.

6   Y. Lin, Y. Liu, D. Zhang, C. Chen and G. Wu, Radiation resistance of poly(methyl methacrylate)/reduced graphene oxide nanocomposites fabricated through latex mixing and in situ reduction, *Chem. Eng. J.*, 2017, **315**, 516–526.

7   M. Altan and H. Yildirim, Mechanical and Antibacterial Properties of Injection Molded Polypropylene/TiO$_2$ Nano-Composites: Effects of Surface Modification, *J. Mater. Sci. Technol.*, 2012, **28**, 686–692.

8   S. Ganguly, P. Bhawal, R. Ravindren and N. C. Das, Polymer Nanocomposites for Electromagnetic Interference Shielding: A Review, *J. Nanosci. Nanotechnol.*, 2018, **18**, 7641–7669.

9   Z. Xu, J. Zhang, M. Shan, Y. Li, B. Li, J. Niu, B. Zhou and X. Qian, Organosilane-functionalized graphene oxide for enhanced antifouling and mechanical properties of polyvinylidene fluoride ultrafiltration membranes, *J. Membr. Sci.*, 2014, **458**, 1–13.

10 S. Liang, K. Xiao, Y. Mo and X. Huang, A novel ZnO nanoparticle blended polyvinylidene fluoride membrane for anti-irreversible fouling, *J. Membr. Sci.*, 2012, **394–395**, 184–192.

11 Z. Yu, X. Liu, F. Zhao, X. Liang and Y. Tian, Fabrication of a low-cost nano-SiO$_2$/PVC composite ultrafiltration membrane and its antifouling performance, *J. Appl. Polym. Sci.*, 2015, **132**, 41267.

12 R. A. Damodar, S.-J. You and H.-H. Chou, Study the self cleaning, antibacterial and photocatalytic properties of TiO$_2$ entrapped PVDF membranes, *J. Hazard. Mater.*, 2009, **172**, 1321–1328.

13 S. Joshi, V. Snehalatha, K. Sivasubramanian, D. Ponraju, V. Jayaraman and B. Venkatraman, Radiation Stability of Epoxy-Based Gamma Shielding Material, *J. Mater. Eng. Perform.*, 2019, **28**, 7332–7341.

14 P. A. O. Muisener, L. Clayton, J. D'Angelo, J. P. Harmon, A. K. Sikder, A. Kumar, A. M. Cassell and M. Meyyappan, Effects of gamma radiation on poly(methyl methacrylate)/single-wall nanotube composites, *J. Mater. Res.*, 2002, **17**, 2507–2513.

15 J. R. Gaier, W. C. Hardebeck, J. R. T. Bunch, M. L. Davidson and D. B. Beery, Effect of intercalation in graphite epoxy composites on the shielding of high energy radiation, *J. Mater. Res.*, 1998, **13**, 2297–2301.

16 U. H. Hossain and W. Ensinger, Decomposition and CO$_2$ evolution of an aliphatic polymer under bombardment with high energy heavy ions, *Polym. Degrad. Stab.*, 2015, **119**, 132–138.

17 R. Thomaz, P. Louette, G. Hoff, S. Müller, J. J. Pireaux, C. Trautmann and R. M. Papaléo, Bond-Breaking Efficiency of High-Energy Ions in Ultrathin Polymer Films, *Phys. Rev. Lett.*, 2018, **121**, 066101.

18 N. Longiéras, M. Sebban, P. Palmas, A. Rivaton and J. L. Gardette, Degradation of epoxy resins under high energy electron beam irradiation: Radio-oxidation, *Polym. Degrad. Stab.*, 2007, **92**, 2190–2197.

19 J. D. Schuler, C. M. Grigorian, C. M. Barr, B. L. Boyce, K. Hattar and T. J. Rupert, Amorphous intergranular films mitigate radiation damage in nanocrystalline Cu-Zr, *Acta Mater.*, 2020, **186**, 341–354.

20 L. Calcagno and G. Foti, Ion irradiation of polymers, *Nucl. Instrum. Methods Phys. Res. Sect. B Beam Interact. Mater. At.*, 1991, **59–60**, 1153–1158.

21 N. J. Briot, M. Kosmidou, R. Dingreville, K. Hattar and T. J. Balk, In situ TEM investigation of self-ion irradiation of nanoporous gold, *J. Mater. Sci.*, 2019, **54**, 7271–7287.

22 R. Ianchis, I. D. Rosca, M. Ghiurea, C. I. Spataru, C. A. Nicolae, R. Gabor, V. Raditoiu, S. Preda, R. C. Fierascu and D. Donescu, Synthesis and properties of new epoxy-organolayered silicate nanocomposites, *Appl. Clay Sci.*, 2015, **103**, 28–33.

23 C. V. More, Z. Alsayed, Mohamed. S. Badawi, Abouzeid. A. Thabet and P. P. Pawar, Polymeric composite materials for radiation shielding: a review, *Environ. Chem. Lett.*, 2021, **19**, 2057–2090.

24 S. Lu, H. Hu, G. Hu and B. Liu, The expression revealing variation trend about radiation resistance of aromatic polymers serving in nuclear environment over absorbed dose, *Radiat. Phys. Chem.*, 2015, **108**, 74–80.

25 F. Rahmani, S. Nouranian, X. Li and A. Al-Ostaz, Reactive Molecular Simulation of the Damage Mitigation Efficacy of POSS-, Graphene-, and Carbon Nanotube-Loaded Polyimide Coatings Exposed to Atomic Oxygen Bombardment, *ACS Appl. Mater. Interfaces*, 2017, **9**, 12802–12811.

26 C. Ashraf, A. Vashisth, C. E. Bakis and A. C. T. van Duin, Reactive Molecular Dynamics Simulations of the Atomic Oxygen Impact on Epoxies with Different Chemistries, *J. Phys. Chem. C*, 2019, **123**, 15145–15156.

27 Y. Xing, Y. Chen, J. Chi, J. Zheng, W. Zhu and X. Wang, Molecular Dynamics Simulation of Cracking Process of Bisphenol F Epoxy Resin under High-Energy Particle Impact, *Polymers*, 2021, **13**, 4339–4351.

28 M. J. Saif, M. Naveed, H. M. Asif and R. Akhtar, Irradiation applications for polymer nano-composites: A state-of-the-art review, *J. Ind. Eng. Chem.*, 2018, **60**, 218–236.

29 S. Nambiar and J. T. W. Yeow, Polymer-Composite Materials for Radiation Protection, *ACS Appl. Mater. Interfaces*, 2012, **4**, 5717–5726.

30 G. Liu, H. Liu, Y. Liu and S. He, The degradation of DGEBA/DICY under 100 keV proton irradiation, *Polym. Degrad. Stab.*, 2011, **96**, 732–738.

31 W. Xia, J. Zhao, T. Wang, L. Song, H. Gong, H. Guo, B. Gao, X. Fan and J. He, Anchoring ceria nanoparticles on graphene oxide and their radical scavenge properties under gamma irradiation environment, *Phys Chem Phys*, 2017, **19**, 16785–16794.

32 S. Chang, J. Li, W. Han, Z. Zhang, L. Chang, W. Chen, Z. Li, Y. Dai and D. Chen, Fabrication and high radiation-resistant properties of functionalized carbon nanotube reinforced novolac epoxy resin nanocomposite coatings, *RSC Adv*, 2016, **6**, 58296–58301.

33 Y. Gao, F. Liu, J. Wang, X. Wang and B. Du, Improvement on Partial Discharge Resistance of Epoxy/Al$_2$O$_3$ Nanocomposites by Irradiation With 7.5 MeV Electron Beam, *IEEE Access*, 2018, **6**, 25121–25129.

34 Y. Gao, J. Wang, F. Liu and B. Du, Surface Potential Decay of Negative Corona Charged Epoxy/Al$_2$O$_3$ Nanocomposites Degraded by 7.5-MeV Electron Beam, *IEEE Trans. Plasma Sci.*, 2018, **46**, 2721–2729.

35 F. Benard, I. Campistron, A. Laguerre and F. Laval, Influence of silica fillers during the electron irradiations of DGEBA/TETA epoxy resins, part I: Study of the chemical modification on model compounds, *Polym. Degrad. Stab.*, 2006, **91**, 2110–2118.

36 R. Li, Y. Gu, Z. Yang, M. Li, S. Wang and Z. Zhang, Effect of γ irradiation on the properties of basalt fiber reinforced epoxy resin matrix composite, *J. Nucl. Mater.*, 2015, **466**, 100–107.

37 M. M. Shameem, S. M. Sasikanth, R. Annamalai and R. G. Raman, A brief review on polymer nanocomposites and its applications, *Mater. Today Proc.*, 2021, **45**, 2536–2539.

38 S. Fu, Z. Sun, P. Huang, Y. Li and N. Hu, Some basic aspects of polymer nanocomposites: A critical review, *Nano Mater. Sci.*, 2019, **1**, 2–30.

39 Vijay Kumar, Balaganesan, Lee, Neisiany, Surendran, and Ramakrishna, A Review of Recent Advances in Nanoengineered Polymer Composites, *Polymers*, 2019, **11**, 644.

40 P. M. Visakh, O. B. Nazarenko, C. S. Chandran, T. V. Melnikova, S. Y. Nazarenko and J.-C. Kim, Effect of electron beam irradiation on thermal and mechanical properties of aluminum based epoxy composites, *Radiat. Phys. Chem.*, 2017, **136**, 17–22.

41 F. Esch, S. Fabris, L. Zhou, T. Montini, C. Africh, P. Fornasiero, G. Comelli and R. Rosei, Electron Localization Determines Defect Formation on Ceria Substrates, *Science*, 2005, **309**, 752–755.

42 Y. Xue, Q. Luan, D. Yang, X. Yao and K. Zhou, Direct Evidence for Hydroxyl Radical Scavenging Activity of Cerium Oxide Nanoparticles, *J. Phys. Chem. C*, 2011, **115**, 4433–4438.

43 P. K. Tewari, *Nanocomposite Membrane Technology: Fundamentals and Applications*, CRC Press, 1st edn., 2015.

44 A. Bedar, R. K. Lenka, N. Goswami, V. Kumar, A. K. Debnath, D. Sen, S. Kumar, S. Ghodke, P. K. Tewari, R. C. Bindal and S. Kar, Polysulfone–Ceria Mixed-Matrix Membrane with Enhanced Radiation Resistance Behavior, *ACS Appl. Polym. Mater.*, 2019, **1**, 1854–1865.

45 J. Chen, B. Liu, X. Gao and D. Xu, A review of the interfacial characteristics of polymer nanocomposites containing carbon nanotubes, *RSC Adv*, 2018, **8**, 28048–28085.

46 H. Zou, S. Wu and J. Shen, Polymer/Silica Nanocomposites: Preparation, Characterization, Properties, and Applications, *Chem. Rev.*, 2008, **108**, 3893–3957.

47 Y. Sun, Z. Zhang, K.-S. Moon and C. P. Wong, Glass transition and relaxation behavior of epoxy nanocomposites, *J. Polym. Sci. Part B Polym. Phys.*, 2004, **42**, 3849–3858.

48 G. Liu, H. Zhang, D. Zhang, H. Zhang, Z. Zhang, X. An and X. Yi, On depression of glass transition temperature of epoxy nanocomposites, *J. Mater. Sci.*, 2012, **47**, 6891–6895.

49 B. Arkles, Tailoring surfaces with silanes, *CHEMTECH*, 1977, **7**, 766–778.

50 D. Liu, A. M. Pourrahimi, R. T. Olsson, M. S. Hedenqvist and U. W. Gedde, Influence of nanoparticle surface treatment on particle dispersion and interfacial adhesion in low-density polyethylene/aluminium oxide nanocomposites, *Eur. Polym. J.*, 2015, **66**, 67–77.

51 M. J. Palimi, M. Rostami, M. Mahdavian and B. Ramezanzadeh, Surface modification of Fe$_2$O$_3$ nanoparticles with 3-aminopropyltrimethoxysilane (APTMS): An attempt to investigate surface treatment on surface chemistry and mechanical properties of polyurethane/Fe$_2$O$_3$ nanocomposites, *Appl. Surf. Sci.*, 2014, **320**, 60–72.

52 T. Rostamzadeh, S. Adireddy, C. D.-W. Chin, M. H. Abdallah and J. B. Wiley, Formation of Mixed-Metal Ceria Nanopeapod Composites within Scrolled Hexaniobate Nanosheets, *ChemNanoMat*, 2019, **5**, 1373–1380.

53 S. J. Blair, B. R. Muntifering, R. O. Chan, C. M. Barr, T. J. Boyle and K. Hattar, Unexpected radiation resistance of core/shell ceramic oxide nanoparticles, *Mater. Today Commun.*, 2018, **17**, 109–113.

54 M. J. Palimi, M. Rostami, M. Mahdavian and B. Ramezanzadeh, Surface modification of Cr2O3 nanoparticles with 3-amino propyl trimethoxy silane (APTMS). Part 1: Studying the mechanical properties of polyurethane/Cr2O3 nanocomposites, *Prog. Org. Coat.*, 2014, **77**, 1663–1673.

55 A. Teleki, N. Bjelobrk and S. E. Pratsinis, Continuous Surface Functionalization of Flame-Made TiO$_2$ Nanoparticles, *Langmuir*, 2010, **26**, 5815–5822.

56 B. Arkles, *Silane Coupling Agents*, Gelest, 2017.

57 J. P. Biersack and J. F. Ziegler, in *Ion Implantation Techniques*, eds. H. Ryssel and H. Glawischnig, Springer Berlin Heidelberg, Berlin, Heidelberg, 1982, pp. 122–156.

58 R. E. Stoller, M. B. Toloczko, G. S. Was, A. G. Certain, S. Dwaraknath and F. A. Garner, On the use of SRIM for computing radiation damage exposure, *Nucl. Instrum. Methods Phys. Res. Sect. B Beam Interact. Mater. At.*, 2013, **310**, 75–80.

59 W. Jiang, M. A. Conroy, K. Kruska, M. J. Olszta, T. C. Droubay, J. M. Schwantes, C. A. Taylor, P. M. Price, K. Hattar and R.

Devanathan, In Situ Study of Particle Precipitation in Metal-Doped CeO_2 during Thermal Treatment and Ion Irradiation for Emulation of Irradiating Fuels, *J. Phys. Chem. C*, 2019, **123**, 2591–2601.

60 A. Y. Konobeyev, U. Fischer, Y. A. Korovin and S. P. Simakov, Evaluation of effective threshold displacement energies and other data required for the calculation of advanced atomic displacement cross-sections, *Nucl. Energy Technol.*, 2017, **3**, 169–175.

61 J. F. Ziegler, M. D. Ziegler and J. P. Biersack, SRIM – The stopping and range of ions in matter (2010), *Nucl. Instrum. Methods Phys. Res. Sect. B Beam Interact. Mater. At.*, 2010, **268**, 1818–1823.

62 Y. Kudriavtsev, A. Villegas, A. Godines and R. Asomoza, Calculation of the surface binding energy for ion sputtered particles, *Appl. Surf. Sci.*, 2005, **239**, 273–278.

63 G. Chen, S. Zhou, G. Gu, H. Yang and L. Wu, Effects of surface properties of colloidal silica particles on redispersibility and properties of acrylic-based polyurethane/silica composites, *J. Colloid Interface Sci.*, 2005, **281**, 339–350.

64 V. Purcar, R. Şomoghi, S. Niţu, C.-A. Nicolae, E. Alexandrescu, I. Gîfu, A. Gabor, H. Stroescu, R. Ianchiş, S. Căprărescu and L. Cinteză, The Effect of Different Coupling Agents on Nano-ZnO Materials Obtained via the Sol–Gel Process, *Nanomaterials*, 2017, **7**, 439.

65 P. Musto, Two-Dimensional FTIR Spectroscopy Studies on the Thermal-Oxidative Degradation of Epoxy and Epoxy–Bis(maleimide) Networks, *Macromolecules*, 2003, **36**, 3210–3221.

66 S. G. Burnay, Radiation-induced changes in the structure of an epoxy resin, *Radiat. Phys. Chem. 1977*, 1980, **16**, 389–397.

67 S. G. Burnay, Radiation induced structural changes in an epoxide resin system—II: Aromatic amine cured system, *Radiat. Phys. Chem. 1977*, 1982, **19**, 93–99.

68 L. Hou, Y. Wu, J. Xiao, B. Guo and Y. Zong, Degeneration and damage mechanism of epoxy-based shape memory polymer under 170 keV vacuum proton irradiation, *Polym. Degrad. Stab.*, 2019, **166**, 8–16.

69 J. R. Lambert, H. F. Shurvell, D. A. Lightner and R. G. Cooks, *Introduction to Organic Spectroscopy*, Macmillan Publishing Company, New York, 1987.

70 B. Mailhot, S. Morlat-Thérias, M. Ouahioune and J.-L. Gardette, Study of the Degradation of an Epoxy/Amine Resin, 1, *Macromol. Chem. Phys.*, 2005, **206**, 575–584.

71 A. Rivaton, L. Moreau and J.-L. Gardette, Photo-oxidation of phenoxy resins at long and short wavelengths—I. Identification of the photoproducts, *Polym. Degrad. Stab.*, 1997, **58**, 321–332.

72 B. Mailhot, S. Morlat-Thérias, P.-O. Bussière and J.-L. Gardette, Study of the Degradation of an Epoxy/Amine Resin, 2: Kinetics and Depth-Profiles, *Macromol. Chem. Phys.*, 2005, **206**, 585–591.

73 M. S. Goyat, A. Hooda, T. K. Gupta, K. Kumar, S. Halder, P. K. Ghosh and B. S. Dehiya, Role of non-functionalized oxide nanoparticles on mechanical properties and toughening mechanisms of epoxy nanocomposites, *Ceram. Int.*, 2021, **47**, 22316–22344.

74 B. J. Ash, L. S. Schadler and R. W. Siegel, Glass transition behavior of alumina/polymethylmethacrylate nanocomposites, *Mater. Lett.*, 2002, **55**, 83–87.

75 M. Xiong, G. Gu, B. You and L. Wu, Preparation and characterization of poly(styrene butylacrylate) latex/nano-ZnO nanocomposites, *J. Appl. Polym. Sci.*, 2003, **90**, 1923–1931.

76 A. Dorigato and A. Pegoretti, Shape memory epoxy nanocomposites with carbonaceous fillers and in-situ generated silver nanoparticles, *Polym. Eng. Sci.*, 2019, **59**, 694–703.

77 M. Preghenella, A. Pegoretti and C. Migliaresi, Thermo-mechanical characterization of fumed silica-epoxy nanocomposites, *Polymer*, 2005, **46**, 12065–12072.

78 M. Rostami, Z. Ranjbar and M. Mohseni, Investigating the interfacial interaction of different aminosilane treated nano silicas with a polyurethane coating, *Appl. Surf. Sci.*, 2010, **257**, 899–904.

79 M. Rostami, M. Mohseni and Z. Ranjbar, An attempt to quantitatively predict the interfacial adhesion of differently surface treated nanosilicas in a polyurethane coating matrix using tensile strength and DMTA analysis, *Int. J. Adhes. Adhes.*, 2012, **34**, 24–31.

80 A. Chatterjee and M. S. Islam, Fabrication and characterization of TiO_2–epoxy nanocomposite, *Mater. Sci. Eng. A*, 2008, **487**, 574–585.

81 Z. Guo, T. Pereira, O. Choi, Y. Wang and H. T. Hahn, Surface functionalized alumina nanoparticle filled polymeric nanocomposites with enhanced mechanical properties, *J. Mater. Chem.*, 2006, **16**, 2800.

82 Z. Guo, K. Lei, Y. Li, H. W. Ng, S. Prikhodko and H. T. Hahn, Fabrication and characterization of iron oxide nanoparticles reinforced vinyl-ester resin nanocomposites, *Compos. Sci. Technol.*, 2008, **68**, 1513–1520.

83 T. Devanne, A. Bry, L. Audouin and J. Verdu, Radiochemical ageing of an amine cured epoxy network. Part I: change of physical properties, *Polymer*, 2005, **46**, 229–236.

84 B. K. Kandola, B. Biswas, D. Price and A. R. Horrocks, Studies on the effect of different levels of toughener and flame retardants on thermal stability of epoxy resin, *Polym. Degrad. Stab.*, 2010, **95**, 144–152.

85 N. Grassie, M. I. Guy and N. H. Tennent, Degradation of epoxy polymers: Part 4—Thermal degradation of bisphenol-A diglycidyl ether cured with ethylene diamine, *Polym. Degrad. Stab.*, 1986, **14**, 125–137.

86 V. Bellenger, E. Fontaine, A. Fleishmann, J. Saporito and J. Verdu, Thermogravimetric study of amine cross-linked epoxies, *Polym. Degrad. Stab.*, 1984, **9**, 195–208.

87 M. Yan, L. Liu, L. Chen, N. Li, Y. Jiang, Z. Xu, M. Jing, Y. Hu, L. Liu and X. Zhang, Radiation resistance of carbon fiber-reinforced epoxy composites optimized synergistically by carbon nanotubes in interface area/matrix, *Compos. Part B Eng.*, 2019, **172**, 447–457.

88 G. Spadaro, S. Alessi and C. Dispenza, *Ionizing radiation-induced crosslinking and degradation of polymers*, Institute of Nuclear Chemistry and Technology: Warsava, Poland, 2017.

89 V. K. Mittal, S. Lotha and D. K. Avasthi, Hydrogen loss under heavy ion irradiation in polymers, *Radiat. Eff. Defects Solids*, 1999, **147**, 199–209.

90 Y. Ngono-Ravache, M. Foray and M. Bardet, High resolution solid-state ^{13}C-NMR study of as-cured and irradiated epoxy resins, *Polym. Adv. Technol.*, 2001, **12**, 515–523.

91 E. Ernault, E. Richaud and B. Fayolle, Thermal oxidation of epoxies: Influence of diamine hardener, *Polym. Degrad. Stab.*, 2016, **134**, 76–86.

92 N. Longiéras, M. Sebban, P. Palmas, A. Rivaton and J. L. Gardette, Multiscale approach to investigate the radiochemical degradation of epoxy resins under high-energy electron-beam irradiation, *J. Polym. Sci. Part Polym. Chem.*, 2006, **44**, 865–887.

93 F. Diao, Y. Zhang, Y. Liu, J. Fang and W. Luan, γ-Ray irradiation stability and damage mechanism of glycidyl amine epoxy resin, *Nucl. Instrum. Methods Phys. Res. Sect. B Beam Interact. Mater. At.*, 2016, **383**, 227–233.

94 A. Rivaton, L. Moreau and J.-L. Gardette, Photo-oxidation of phenoxy resins at long and short wavelengths—II. Mechanisms of formation of photoproducts, *Polym. Degrad. Stab.*, 1997, **58**, 333–339.

95 F. Djouani, Y. Zahra, B. Fayolle, M. Kuntz and J. Verdu, Degradation of epoxy coatings under gamma irradiation, *Radiat. Phys. Chem.*, 2014, **82**, 54-62.

96 C. T. Ratnam, M. Nasir, A. Baharin and K. Zaman, Electron beam irradiation of epoxidized natural rubber: FTIR studies, *Polym Int*, 2000, 9.

97 U. H. Hossain, V. Lima, O. Baake, D. Severin, M. Bender and W. Ensinger, On-line and post irradiation analysis of swift heavy ion induced modification of PMMA (polymethyl-methacrylate), *Nucl. Instrum. Methods Phys. Res. Sect. B Beam Interact. Mater. At.*, 2014, **326**, 135–139.

98 X. Zhang, K. Hattar, Y. Chen, L. Shao, J. Li, C. Sun, K. Yu, N. Li, M. L. Taheri, H. Wang, J. Wang and M. Nastasi, Radiation damage in nanostructured materials, *Prog. Mater. Sci.*, 2018, **96**, 217–321.

99 B. J. Cowen, M. S. El-Genk, K. Hattar and S. A. Briggs, Investigations of irradiation effects in crystalline and amorphous SiC, *J. Appl. Phys.*, 2019, **126**, 135902.

100 I. J. Beyerlein, A. Caro, M. J. Demkowicz, N. A. Mara, A. Misra and B. P. Uberuaga, Radiation damage tolerant nanomaterials, *Mater. Today*, 2013, **16**, 443–449.

101 A. Misra, M. J. Demkowicz, X. Zhang and R. G. Hoagland, The radiation damage tolerance of ultra-high strength nanolayered composites, *JOM*, 2007, **59**, 62–65.